



Seismogenic potential and tsunami threat of the strike-slip Carboneras Fault in the Western Mediterranean from physics-based earthquake simulations

José A. Álvarez-Gómez¹, Paula Herrero-Barbero¹, and José J. Martínez-Díaz^{1,2}

¹Department of Geodynamics, Stratigraphy and Palaeontology. Faculty of Geology. Complutense University of Madrid, Madrid, Spain

²IGEO, Geosciences Institute, CSIC-UCM, Madrid, Spain

Correspondence: José A. Álvarez-Gómez (jaag@ucm.es)

Abstract. Strike-slip fault ruptures have a limited capacity to generate vertical deformation, and for this reason they are usually dismissed as potential destructive tsunami sources. At the western tip of the western Mediterranean, in the Alboran Sea, tectonics is characterized by the presence of large transcurrent fault systems and minor reverse and normal faults in a zone of diffuse deformation. The strike-slip Carboneras fault is one of the largest sources in the Alboran Sea, and therefore, with the greatest seismogenic capacity. It is also one of the active structures with higher slip rates in the Eastern Betic Fault Zone and has been proposed as source of the damaging 1522 (M6.5; Int. VIII-IX) Almeria earthquake. The dimensions and location of the Carboneras fault imply a high seismic and tsunami threat. In this paper we present tsunami simulations from seismic sources generated with physics-based earthquake simulators. We have generated a 1 Myr synthetic seismic catalogue consistent on 773,893 events with magnitudes ranging between M_W 3.3 and 7.6. From these events we have selected those sources producing a potential energy capable of generating a noticeable tsunami, being earthquakes with magnitudes ranging from 6.71 to 7.62. The Carboneras Fault has the capacity to generate locally damaging tsunamis, however, on a regional scale its tsunami threat is limited. The frequency – magnitude distribution of the generated seismic catalogue reflects the variability of magnitudes associated to the rupture of the entire fault, departing the upper limit from the classical Gutenberg-Richter potential relation showing a bell-shaped distribution. The inter-event time for the maximum earthquake magnitudes is usually between 2000 and 6000 years. The use of physics-based earthquake simulations for tsunamigenic sources allows a robust characterization of the scenarios, allowing a qualitative leap in their parametrization.

1 Introduction

Tsunamis are generated by any natural event that involves an immediate alteration of the elevation of the free surface of the sea. This alteration may be due to events that directly alter the sea surface (usually meteorological, meteoric or volcanic events) or by geological events that abruptly modify the ocean floor (earthquakes or submarine landslides). Earthquakes are the geological events that most often generate destructive tsunamis (NGDC, 2022), and this ability depends on their mode of seismic rupture (e.g., Burbidge et al., 2015; Geist, 1998; Gibbons et al., 2022). The rake, the orientation of the slip vector on



the fault plane during seismic rupture, is one of the most determining parameters in the generation of tsunamis, presenting the thrust and normal faults, with dip-slip rupture, the greatest capacity. On the other hand, the strike-slip ruptures, with rakes close to the horizontal, have a limited capacity to generate vertical deformation on the seafloor, and for this reason they are usually dismissed as potential destructive tsunami sources.

Although the lower capacity of strike-slip faults to generate tsunamis is a proven fact, it is not negligible, as has been numerically demonstrated (Elbanna et al., 2021; Legg et al., 2003; Tanioka and Satake, 1996; Ulrich et al., 2019) and observed (Frucht et al., 2019; Gusman et al., 2017; Heidarzadeh et al., 2017; Ho et al., 2021), occasionally linked to submarine landslides also (Hornbach et al., 2010; Xu et al., 2022). This is of special relevance in local sources, where the dispersion of the tsunami waves is low, and the local fault complexities and rupture-slip variations are key parameters on tsunami impact (Geist, 2002).

The study of tsunami hazard, due to the scarcity of events from a statistical point of view, is frequently approached from numerical modelling. These models are usually based on the simulation of tsunamis generated by ruptures of simple, rectangular, fault planes with homogeneous slip. Codes based on the Okada (1985) or Mansinha and Smylie (1971) equations are used to obtain the seafloor deformation produced by the earthquake.

However, the variability in the slip distribution on the fault plane is a fundamental parameter to understand the occurrence of maximum amplitudes in destructive events (Fujii et al., 2011; Gusman et al., 2012; McCloskey et al., 2008; Satake et al., 2013; Yamazaki et al., 2011). This variability is of special relevance in local sources, which if modelled as simple ruptures, cannot capture the complexity of the earthquake rupture process. Wave propagation and flooding are highly non-linear processes, very sensitive to local variations in shallow waters. To overcome this limitation, methodologies have been proposed based on the stochastic (or random) generation of slip patterns in faults (Goda et al., 2015; Lavallée et al., 2006; Løvholt et al., 2012; Mai and Beroza, 2002), or on the use of physical dynamic rupture models for particular events (Elbanna et al., 2021; Kozdon and Dunham, 2013; Madden et al., 2021; Maeda and Furumura, 2013; Ryan et al., 2015; Wendt et al., 2009; Wilson and Ma, 2021).

Our approach is based on the use of physics-based earthquake simulators (Rundle, 1988). These simulators have been developed in recent decades in order to overcome the temporal limitation of the instrumental seismic catalogue in probabilistic seismic hazard assessment (PSHA) (Robinson et al., 2011; Shaw et al., 2018), especially in the characterization of large events. Through the development of models based on earthquake physics, synthetic catalogues of hundreds of thousands of years can be generated whose characteristics reflect those of the instrumental catalogue but incorporating the long-term evolution of the seismic cycle and the complex interactions of fault systems (Console et al., 2018, 2015; Robinson and Benites, 1995). Moreover, recent development of numerical codes based on the rate-and-state constitutive law for fault slip and frictional behaviour (Dieterich, 1992, 1995) allows not only the modelling of long-term seismic cycle deformation, but also the short-term rupture process based on a quasi-dynamic physical approximation to the rupture propagation (Richards-Dinger and Dieterich, 2012) producing earthquake ruptures similar to those in fully dynamic models (Whirley and Engelmann, 1993).

The western Mediterranean presents a complex tectonic history and context (e.g. Chertova et al., 2014; Gómez de la Peña et al., 2021; Romagny et al., 2020); and is characterized by the development of a series of arcuate Fold-and-Thrust Belts surrounding back-arc formed deep-water basins (Faccenna et al., 2004; Rosenbaum and Lister, 2004). The current rate of shortening between the Nubian and Eurasian plates in the western Mediterranean is approximately 5 mm/yr (Serpelloni et al.,

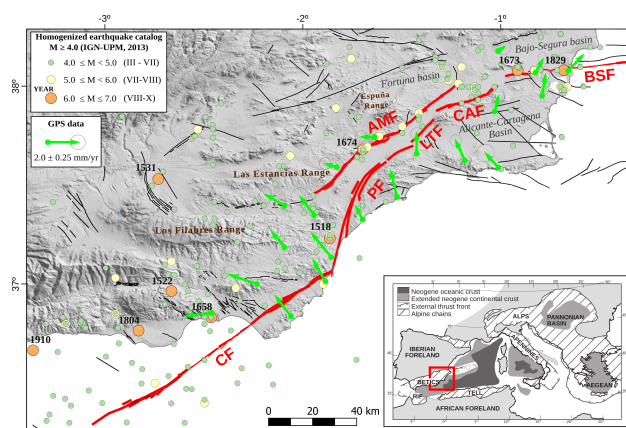


Figure 1. Seismotectonic setting of the Eastern Betic Shear Zone (EBSZ), modified from Herrero-Barbero et al. (2021). The filled circles show the epicentres of the **homogenized earthquake catalogue** from the IGN-UPM (2013). The green arrows represent geodetic velocities from GNSS networks (Borque et al., 2019; Echeverría et al., 2013) with Eurasia-fixed reference frame. Fault traces from the Quaternary Active Fault Database of Iberia, QAFI v.3 (García-Mayordomo et al., 2017). In red the main faults of the EBSZ: Carboneras fault (CF), Alhama de Murcia fault (AMF), Palomares fault (PF), Los Tornos fault (LTF), Carrascoy fault (CAF), and Bajo-Segura fault (BSF). The inset shows the location of the EBSZ in the western tip of the Alpine orogenic belt (modified from Martínez-García (2012)).

2007; Vernant et al., 2010), **which, being distributed** in a large number of structures, makes them to have low or very low velocities. These low deformation rates imply that the seismic cycles of the main structures are very long and the instrumental seismic catalogue can hardly show the characteristics of the potential major events.

At the western tip of the **western** Mediterranean, in the Alboran Sea, tectonics is characterized by the presence of large transcurrent fault systems and minor reverse and normal faults in a zone of diffuse deformation (Ballesteros et al., 2008; Martínez-García et al., 2013). These structures, formed during the Miocene in a transcurrent and mainly extensional tectonic context, were latter reactivated in a transpressional post-tortonian setting (Bourgeois et al., 1992; Comas et al., 1992; Do Couto et al., 2016; Herrero-Barbero et al., 2020; Martínez-García et al., 2017). Although the reverse faults associated with the Alboran ridge seem to have the greatest tsunamigenic potential (Álvarez-Gómez et al., 2011a, b; Gómez de la Peña et al., 2022), the mainly strike-slip faults (Yusuf, Al -Idrisi and Carboneras) are the ones with the greatest length and, therefore, the greatest seismogenic capacity (Somoza et al., 2021).

The Carboneras fault is a left-lateral transpressive structure oriented N50-60°E with a length of ~ 150 km, most of them offshore (Gràcia et al., 2006; Somoza et al., 2021). It is one of the active structures with higher slip rates in the Alboran Sea and in the Eastern Betic Shear Zone (Masana et al., 2018; Moreno et al., 2015), a fault system that crosses the SE of the Iberian Peninsula forming a tectonic corridor on which a significant density of population and industry is based (Figure 1). Moreover this fault has been proposed as source of the 1522 **Almería** earthquake, a damaging earthquake that reached **intensities** of VIII-IX in the city of Almería (Martínez Solares and Mezcua, 2002), and possibly related to a local tsunami (Reicherter and Hübscher, 2007; Reicherter and Becker-Heidmann, 2009).



The dimensions and location of the Carboneras fault poses a high seismic and tsunami risk potential. According to previous studies this fault has the capacity to produce events with magnitudes up to 7.1 - 7.4 (Álvarez-Gómez et al., 2011a; García-Mayordomo et al., 2017; Gómez de la Peña et al., 2022; Gràcia et al., 2006) with mainly horizontal left-lateral component but some reverse dip-slip motion too (Moreno et al., 2015). Although the tsunami simulations done to date (Álvarez-Gómez et al., 2011a, b; Gómez de la Peña et al., 2022) discard major damaging events, the simplicity and assumptions of such simulations must be re-evaluated.

In this paper we present tsunami simulations based on the generation of a synthetic catalogue of earthquakes whose characteristics resemble the instrumental and historical seismicity recorded in the area (Herrero-Barbero et al., 2021). From these simulations we make estimates of maximum wave elevations for seismogenic tsunamis and recurrence intervals for significant events in order to reassess the threat posed by the Carboneras fault in the context of the Alboran Sea and the western Mediterranean.

2 Earthquake ruptures simulation

Reproducing a long-term catalogue of earthquake ruptures requires a computationally efficient approach to the physical processes that control earthquake occurrence. Earthquake simulators (Rundle, 1988; Tullis et al., 2012; Ward, 2000) are computer codes that use fault geometry, stress interactions and frictional resistance to produce long earthquake sequences, overcoming the completeness limitations of the instrumental record. The multi-cycle earthquake simulations necessarily adopt approximations to elastodynamics to make computation feasible and, unlike fully dynamic single-event simulators (see e.g., Harris et al., 2018), seismic waves are not computed. Even so, recent modelling enhancements have successfully extended their use in more complex fault geometries (Field et al., 2014; Shaw et al., 2018) and for different representations of fault friction, rheology and stress transfer (Pollitz, 2012; Richards-Dinger and Dieterich, 2012; Sachs et al., 2012; Schultz et al., 2018; Ward, 2012); therefore, a better validation of the quasi-dynamic part of the seismic cycle is achieved.

Our approach is based on the application of the RSQSim earthquake simulator (Dieterich and Richards-Dinger, 2010; Richards-Dinger and Dieterich, 2012). The physics-based RSQSim code reproduces earthquakes into a fully interacting 3D fault model. It performs the physical processes leading rupture nucleation and propagation through a boundary element formulation that incorporates rate- and state-dependent friction based on Dieterich (1995). Given that this is a quasi-dynamic approximation, long-term stress accumulation and earthquake slip at each fault element is separated efficiently into three sliding states: 0) locked, 1) nucleating, and 2) sliding. The result is a long synthetic earthquake catalogue including a comprehensive and detailed record of complex earthquake ruptures with heterogeneous slip. Recent results obtained using the RSQSim code are promising in relation to potential practical applicability (Chartier et al., 2021; Herrero-Barbero et al., 2021; Howarth et al., 2021; Shaw et al., 2018).

The 3D structure of the Carboneras fault is integrated in a more complex fault model of the Eastern Betic Fault Zone (Figure 2), which includes kinematic properties of the main faults, such as slip rates and rakes (Herrero-Barbero et al., 2021). RSQSim simulations have been run on this fault system model of triangular elements with 1 km² resolution and fault depths between

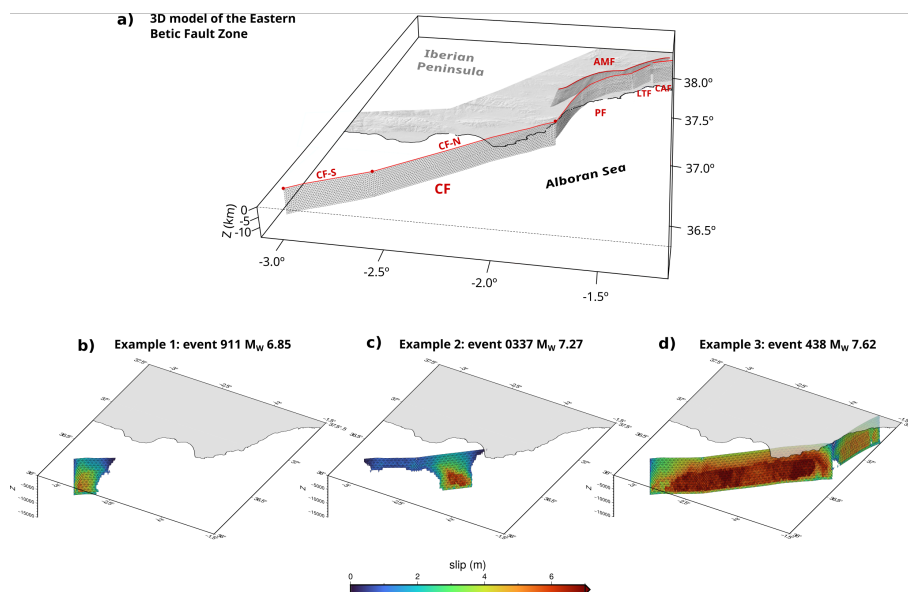


Figure 2. a) 3D fault model used for the synthetic seismic catalogue simulation; b) example of a M_W 6.85 event; c) example of a M_W 7.27 event; d) example of a M_W 7.62 event.

8 and 12 km. The Carboneras fault is defined in the model as a sub-vertical (dipping 85° SE) sinistral strike-slip structure (Bousquet, 1979; Masana et al., 2018; Moreno et al., 2015; Rutter et al., 2012), $N45^\circ$ - 60° strike, and segmented into two fault sections: an onshore northern section, partially offshore at the SW and connecting with the Palomares fault at the NE; and a totally offshore southern section. In the northern Carboneras fault, an average lateral slip rate of 1.2 mm/yr is estimated for the last 110-130 ka (Moreno et al., 2015). In the southern section Moreno (2011) estimated a strike-slip rate of 1.3 mm/yr, which is consistent with the northern section and with geodetic lateral slip rates of 1.3 ± 0.2 mm/yr (Echeverria et al., 2015).

Besides the input kinematic data, the simulations are governed by rate- and state-dependent friction parameters, a and b , that reproduce the effect of the velocity-change on the coefficient of friction (Dieterich, 1979; Ruina, 1983). These frictional parameters have a notable impact on the slip distribution and spatio-temporal clustering (Noda and Lapusta, 2013; Richards-Dinger and Dieterich, 2012; Scholz, 1998). We define reference rate-and-state values based on experimental data taken from a nearby location in the fault zone (Niemeijer and Vissers, 2014; Rodriguez Escudero, 2017) to generate multiple test catalogues. The aims of the testing process were to match frequency distributions with a Gutenberg-Richter b value close to 1.0 ± 0.1 , and to correlate the synthetic seismicity with instrumental and paleoseismic data (Herrero-Barbero et al., 2021). Finally, a preferred set of input model parameters is selected for the best-fit catalogue: rate-and-state friction parameters $a=0.001$ and $b=0.010$; a steady-state friction coefficient $\mu_0=0.6$; a depth-variable normal stress with a 20 MPa/km gradient, and a b -value of 1.05 (Figure 3). Defined frictional parameters in this study entail a totally seismogenic behaviour of this fault system, although Faulkner et al. (2003) also suggested possible creeping sections in the Carboneras fault zone due to the mechanical heterogeneity of its fault gouge.

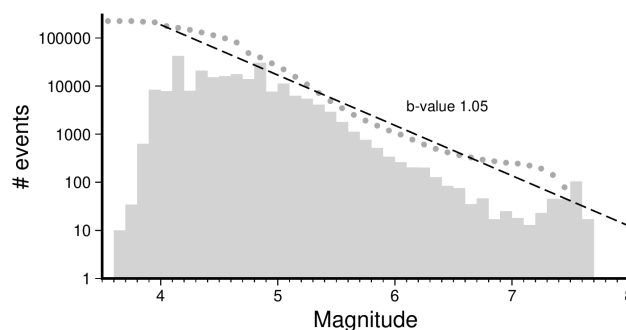


Figure 3. Frequency magnitude distribution of the generated synthetic earthquake catalogue for the Carboneras Fault. The grey bars show the discrete count of events, while the grey dots show the cumulative form of the distribution. The dashed line shows the best fit of the Gutenberg-Richter law.

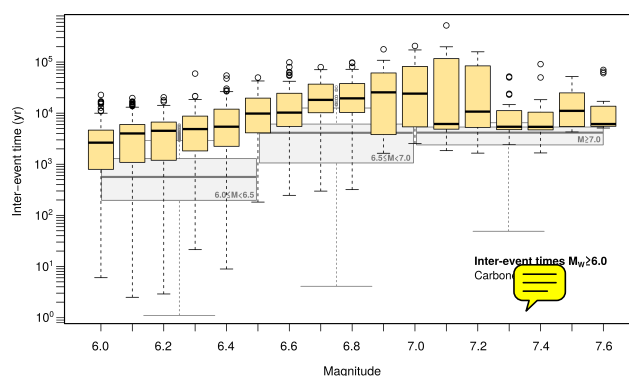


Figure 4. Inter-event time distribution. The graph shows a box and whisker plot for intervals of 0.1 in magnitude in yellow. In grey are shown box and whisker plots for different magnitude ranges.

According to the selected input model parameters, a 1 Myr-synthetic earthquake catalogue has been generated (Figure 3), from which the first 2000 years have been discarded to avoid artefacts until the simulation stabilizes. In total, 773,893 events have been obtained, with a magnitude range of $3.3 \leq M_W \leq 7.6$. The Carboneras Fault is the seismogenic source that generates the most frequent synthetic seismicity, with almost a 30% of the events in the catalogue, of which 0.6% of total events are $M_W \geq 6$ earthquakes. For $6.5 \leq M_W < 7.0$ events, the most frequent inter-event time intervals range between 800 and 6,000 years (Figure 4), **excluding the aftershocks**. Logically, the earthquake frequency decreases as the magnitude increases (Figure 4). However, from magnitude M_W 7.0-7.1, the simulation shows an increase in the frequency of events, therefore the recurrence intervals of the most damaging $M_W \geq 7.0$ earthquakes would be shortened. The largest number of these major simulated ruptures in the Carboneras Fault **is** nucleated in the northern section, being physically capable to propagate a complete fault-length rupture. Between them, 115 ruptures are also transferred to a portion of the southern branch of the Palomares Fault (Figure 2d), increasing the rupture area and therefore the released seismic moment.

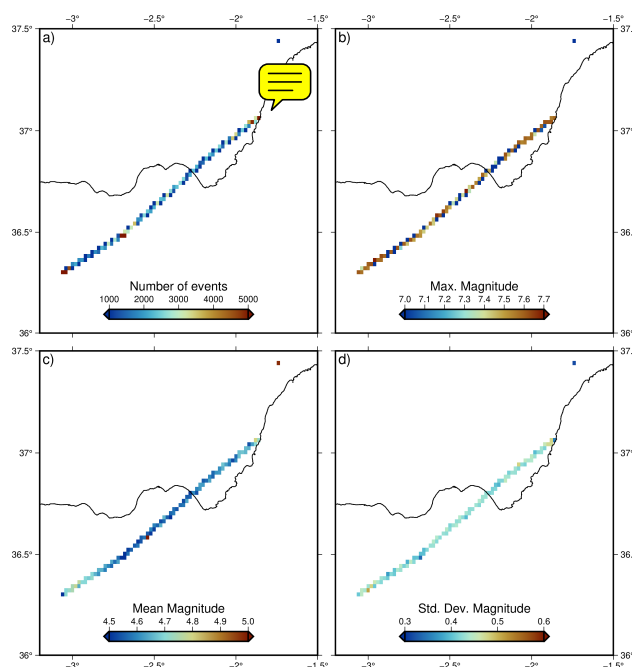


Figure 5. Different statistics for the epicentral location of the modelled events shown as heat maps with a cell size of $\sim 5 \text{ km}^2$. a) Number of epicentres; b) maximum magnitude; c) mean magnitude; d) magnitude standard deviation.

The epicentres of the generated events are not homogeneously distributed along the fault; being more frequent the generation of events at the tips of the sections and bending (Figure 5a). Towards the ends of the fault is also where the average magnitude is higher (Figure 5c). However, the maximum magnitude of the generated event does not show an important variation; being generated events with magnitudes $M > 7.3$ along the entire fault trace (Figure 5b).

3 Tsunami modelling

Simulations for seismic triggered tsunamis are based on modelling the deformation of the ocean bottom produced by the earthquake rupture. These models use analytical solutions in an elastic half-space to reproduce the behaviour of the upper crust. The most commonly used codes for this are often based on equations derived for rectangular dislocations (Mansinha and Smylie, 1971; Okada, 1985, 1992), which makes it difficult to model complex rupture geometries without incorporating numerical artefacts. To solve this problem other mathematical approaches and alternative algorithms have been developed, also using analytical equations, but for triangular dislocations (Gimbutas et al., 2012; Meade, 2007; Nikkhoo and Walter, 2015). In this work we have used the calculation algorithm developed by Nikkhoo and Walter (2015) for artefact-free triangular geometries.

To evaluate the potential of tsunami generation of the modelled earthquakes, we have initially selected events with magnitudes greater than 6.0; obtaining a total of 1344 events. Many of these events will not have the capacity to generate detectable



tsunamis on the coast, so to avoid an excessive computational load, we have filtered these pre-selected events based on the surface deformation generated. As the sea-floor deformation generated by the earthquake is usually transferred instantly to the elevation of the water free surface we can use it to directly estimate the event capacity to generate a tsunami.

Each earthquake rupture is characterized by its unique finite fault model composed by a number of triangular elements. The smaller events considered here, with magnitudes 6.0, are formed by a few tens of elements (~ 40); while the biggest ones, with magnitudes of ~ 7.6 are formed by the rupture of a few thousands of elements (up to 5279). In total we have modelled the rupture of 1150265 triangular elements for the 1344 finite fault models.

We have parametrized each sea-floor deformation modelled with the following quantities (Bolshakova and Nosov, 2011; Wessel, 1998) (Figure 6):

i) maximum uplift or water elevation

$$\eta_{max} = \max[\eta_Z(x, y)] \quad (1)$$

ii) maximum vertical displacement double-amplitude defined as

$$A_\eta = \max[\eta_Z(x, y)] - \min[\eta_Z(x, y)] \quad (2)$$

iii) displaced volume

$$V = \iint_S |\eta_Z(x, y)| dS \quad (3)$$

and iv) potential energy

$$E_{ts} = \frac{1}{2} \rho g \iint_S \eta_Z^2(x, y) dS \quad (4)$$

where ρ is the density of water (taken as 1038 kg/m^3 (Borghini et al., 2014)) and g the acceleration due to gravity.

Nosov et al. (2014) analysed a series of tsunamis generated by earthquakes whose source were characterized with a finite fault model. They compared the modelled surface deformation with the size and intensity of the generated tsunami. Based on these data, they established a series of relationships between the Soloviev-Imamura intensity of the tsunami (Gusiakov, 2011) and different parameters of the sea-floor deformation, among them the displaced volume and the potential energy. Figure 6a shows the ranges of intensity values defined as a function of the potential energy:

$$i = 1.16 \log_{10}(E_{ts}) - 14.2 \quad (5)$$

We have selected to simulate those events with a potential energy capable of generating a tsunami of intensity of at least -2. This criteria restricts the number of tsunami propagations to model from 1344 events with $M > 6$ to 331 events with earthquake magnitudes ranging from 6.71 to 7.62 and double amplitudes A_η from 0.3 m to 1.2 m.

Bolshakova and Nosov (2011) examined some relevant tsunamis for which they also parametrized the sea-floor deformations. It is noteworthy that those events with double amplitudes below 0.4 m were only perceptible in tide gauges, not generating a

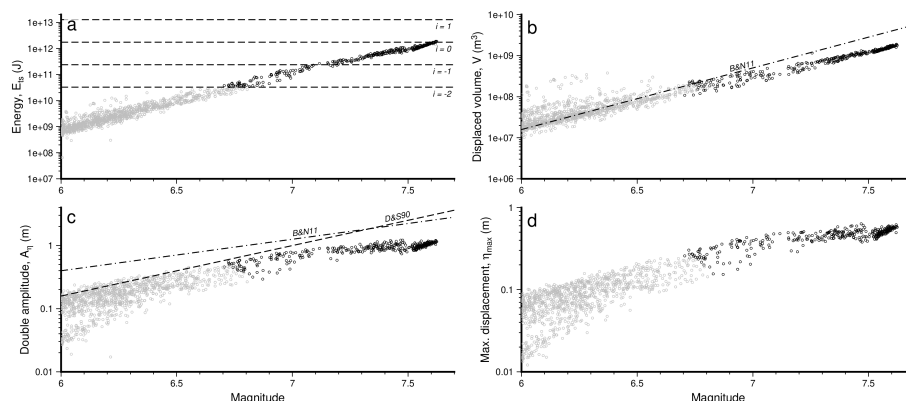


Figure 6. Relations of seafloor deformation parameters with earthquake magnitude. a) Potential energy. Dashed lines show the tsunami intensity according to equation 5. b) Displaced volume. Dash-dotted line shows the Bolshakova and Nosov (2011) upper limit for the magnitude - volume relation. c) Displacement double amplitude. Dash-dotted line shows the Bolshakova and Nosov (2011) upper limit for the magnitude - double amplitude relation and the dashed line the Dotsenko and Soloviev (1990) empirical relation. d) Maximum vertical displacement.

notable impact on the coast. As can be seen in Figure 6 there is a good correspondence between the events selected to simulate with those whose double amplitudes are above 0.3 - 0.4 m.

In order to model the tsunami propagation we have resort to the highly used and validated code COMCOT (Cornell Multi-
 185 grid Coupled Tsunami) (Liu et al., 1995; Wang and Liu, 2006). This algorithm is based on the Non-linear Shallow Water Equations built over a modified leap-frog nested grids scheme.

The bathymetry used is composed of three independent sources (Figure 7). On the one hand, the bathymetric data corresponds to the EMODnet 2020 mesh (EMODnet, 2022), with a horizontal resolution of 1/16' (~115 m). On the other hand, for the regional topography, we have used the MERIT global DEM (Yamazaki et al., 2017), with a horizontal resolution of 3"
 190 (~90 m). For the highest resolution mesh, on the coast of Almeria, we have used the topography of the digital model of 25 m from the National Geographic Institute of Spain (CNIG, 2022). The regional mesh has been resampled with a cell size of 500 m and the local one with 100 m.

For each of the 331 tsunami propagations we have computed the maximum elevation for a model running during 90 minutes, which is enough time for the waves to propagate through the basin and capture the wave reflections. In Figure 8 tsunami travel
 195 times are shown as well as examples of the results for three events with different magnitudes.

As expected, for the smaller magnitude events, the location of the rupture, as well as the slip distribution along the fault plane, are the determining factor in the location of the maximum wave elevations (Figure 8a-d). However, for the maximum events (Figures 8e-f), in which slip occurs along the entire fault plane (see Figure 2d), the location of the maximum wave elevations are clearly determined by the morphology of the sea-floor.

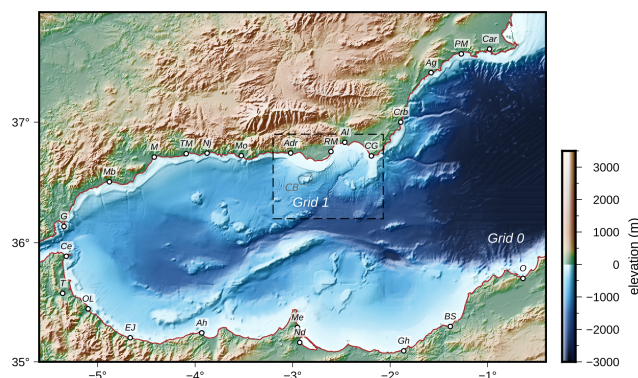


Figure 7. Bathymetric grids used in the propagation modelling. The Grid 0, with a cell size of 500m is composed by the EMODnet 2020 bathymetry (EMODnet, 2022) and the topography by the MERIT DEM (Yamazaki et al., 2017). The Grid 1, with a cell size of 100m, is composed by the EMODnet bathymetry and the 25 m resolution topographic DEM of the IGN (CNIG, 2022). The dashed polygon labelled with CB marks the location of the Chella Bank bathymetric feature. The labels show the main localities mentioned in the text: Car, Cartagena; PM, Puerto de Mazarron; Ag, Aguilas; Crb, Carboneras; CG, Cabo de Gata; Al, Almeria; RM, Roquetas de Mar; Adr, Adra; Mo, Motril; Nj, Nerja; TM, Torre del Mar; M, Malaga; Mb, Marbella; G, Gibraltar; Ce, Ceuta; T, Tetouan; OL, Oued Laou; EJ, El Jebha; Ah, Al Hoceima; Me, Melilla; Nd, Nador; Gh, Ghazaouet; BS, Beni Saf; O, Oran.

200 The classical tsunami hazard deterministic approach consist on the definition of the worst-case scenario based on the dimensions of the source and the employ of a series of empirical relations to define the magnitude of the event and the average slip over the fault. Alternatively, instead of defining a single average homogeneous slip model, a set of stochastic variable slip models can be produced and analysed statistically.

A common procedure is to show the maximum wave elevation expected for each model cell from a series of modelled
 205 sources. This kind of map is usually called aggregated maximum elevation map; and is very useful to determine the worst impact of the wave considering all the potential sources. An extension of this reasoning is the aggregation of maximum elevations produced by a set of tsunamis produced by variable slip models on a single source or a set of sources. With this latter approach we have produced the aggregated maximum elevation map shown in Figure 9.

The maximum elevations produced by the Carboneras strike-slip fault exceed 1 m consistently, and with relevant inundations,
 210 in the Almerian coast (Figure 9). The maximum elevations are located in front of the fault rupture, from Adra to Almeria city, but with relevant local inundations in the Cabo de Gata area. Towards the west the maximum elevations can reach locally 1 m but usually show values of a few decimetres. In the opposite coast, in northern Africa, the maximum elevations are always in the range of 0.1 - 0.8 m with the highest values from Melilla to Ghazouet. For north Africa only the coarse bathymetry has been used and local reflections and resonances not modelled could produce higher elevations locally.

215 Having produced hundreds of rupture scenarios that obey both dimensional and temporal characteristics to the regional seismotectonic context, we can statistically analyse the propagation results. For each calculation point on the map we obtain a statistical distribution of elevations. In Figure 10 some examples are shown for localities along the coast. These elevations

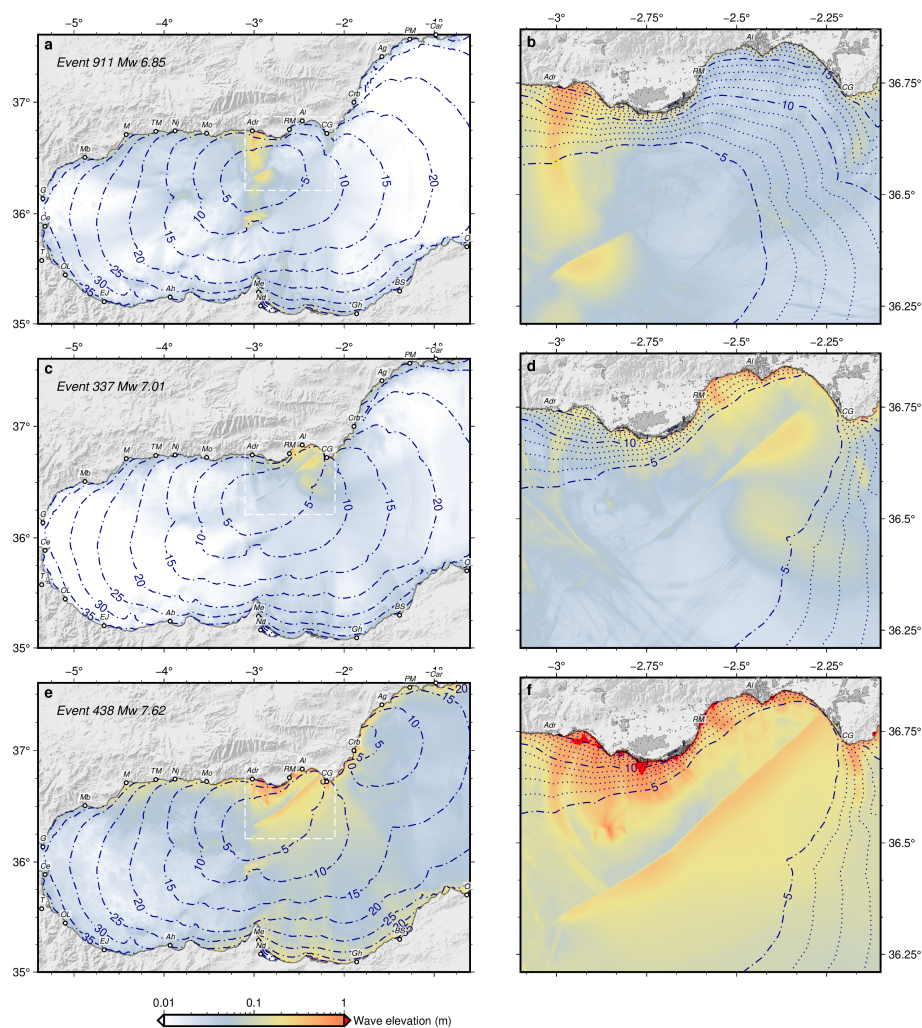


Figure 8. Example of maximum wave elevations obtained for three events (out of 331) with different magnitudes. The ruptures corresponding with these events are shown in Figure 2. See Figure 7 for labels of localities.

have been taken for the 5 m depth isobath. The distribution shown is common for the entire calculation domain, where several local maxima in the distribution can be interpreted, being far from a normal distribution. The highest frequency is commonly related with the lower elevation values, denoting the lower recurrence interval of small events. The second peak observed is usually related to the highest wave elevations, with values ranging from 1.2 m to 2 m. In some places these higher elevations constitute the most frequent values (as is seen in the example of Figure 10a, corresponding to the locality of Adra). Between these two local maxima in the distribution two more local peaks can be interpreted, although of less importance.

In a simple way we have decided to show the statistical complexity of the distributions of maximum elevations on the coast through the use of quartiles; thus Figure 11 shows the maximum elevations corresponding to the 25%, 50% (median) and

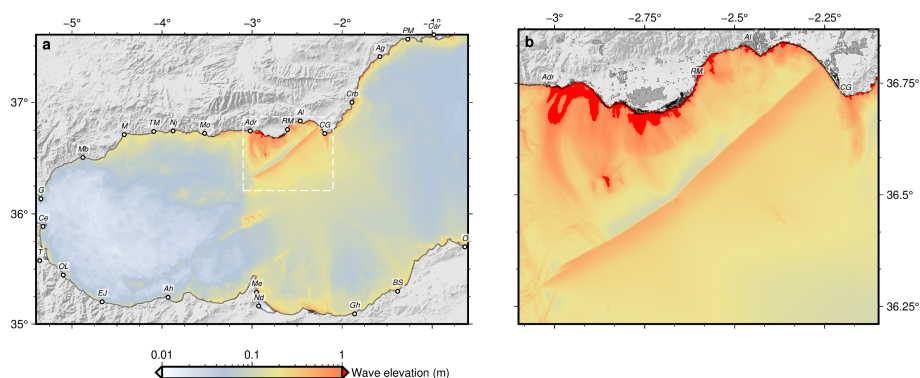


Figure 9. Maximum wave elevation aggregated a) regional and b) local maps. See Figure 7 for labels.

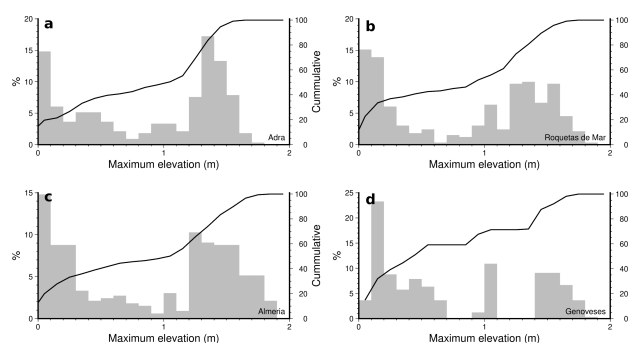


Figure 10. Tsunami wave maximum elevations frequency distribution for locations in a) Adra; b) Roquetas de Mar; c) Almería and d) Genoveses Cove.

75% quartiles. The difference between the regional and local maximum elevations arise from the different cell size used in the propagation modelling. The regional bathymetry (grid 0 in Figure 7) has a cell size of 500m, while the local bathymetry (grid 1) has a cell size of 100 m. The coarser bathymetry is unable to reproduce with precision the nearshore complexities and the maximum wave elevations are underestimated. This is clearly shown in the 75% quartile maximum elevations (Figure 11c,f), where the elevations along the coast are consistently higher using the local bathymetry compared with the regional. A specially illustrative example is shown in the area of Cabo de Gata (near the eastern edge of the local grid); where a peak on the elevation stands out. This peak is located in the Genoveses cove (Figures 11f) where resonance effects are probably responsible of exceptionally high elevations.

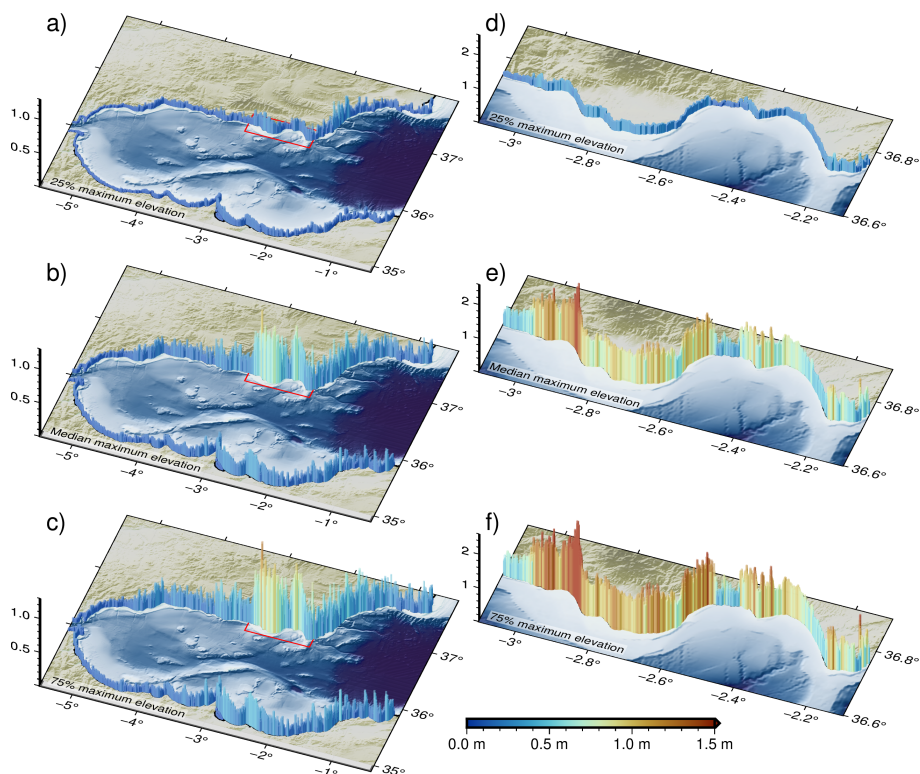


Figure 11. Quartiles of maximum wave elevations obtained from the set of modelled sources. Regional scale maps for a) 25% quartile; b) 50% quartile and c) 75% quartile. Local scale maps for d) 25% quartile; e) 50% quartile and f) 75% quartile.

4 Discussion

235 Tsunamigenic potential of the Carboneras Fault

In line with results obtained in previous analyses of the tsunamigenic potential of strike-slip faults (Elbanna et al., 2021; Frucht et al., 2019; Gusman et al., 2017; Heidarzadeh et al., 2017; Ho et al., 2021); this work demonstrates the tsunamigenic capacity of the Carboneras Fault. This is a strike-slip fault, with some dip-slip component (rake $\sim 10^\circ$ based on field analysis of its outcrops onshore according to (Moreno et al., 2015) and with the capacity to generate locally damaging tsunamis. However, on a regional scale considering the Alboran Sea basin, its tsunamigenic capacity is more limited, being able to produce tsunamis of small entity in the North African coast between Melilla and Ghazaouet (Figure 9) although with a low frequency (Figure 11).

If we compare the results of this work with previous results (Álvarez-Gómez et al., 2011a, b; Gómez de la Peña et al., 2022) we can see that the tsunamigenic capacity modelled here is higher. While the fault geometry is essentially the same with minor variations due to the higher resolution and fidelity used in our models than in those of Álvarez-Gómez et al. (2011a) and Gómez de la Peña et al. (2022), there are other parameters that differ significantly. The maximum magnitude, estimated according to



empirical relationships, in previous models was M_W 7.1 - 7.2, notably lower than the maximum magnitude reached with our physical model, M_W 7.62, which is close to the maximum magnitude proposed by Moreno (2011). This difference in magnitude consequently produces an important difference in net slip. The one used by Álvarez-Gómez et al. (2011a) is 1.9 m and 1.38 m by Gómez de la Peña et al. (2022); these being average slips over the entire rupture area. In the models that we have developed in this work, the slip is variable, but the average slip for a worst-case of magnitude 7.62 would be ~ 6 m, with maximum slips ~ 9 m. On the other hand, the rake used in our models is 10° while Álvarez-Gómez et al. (2011a) used 15° and Gómez de la Peña et al. (2022) used 0° .

Seismogenic potential and Frequency-Magnitude distribution

Although the difference in maximum magnitudes may seem large, it must be taken into account that those provided by the empirical relations are the mean values of the regressions best fits, with standard deviations that may be high. On the other hand, in our models we have selected the largest magnitude generated throughout a 1 Myr. catalogue; and not the average value of the maximum magnitudes generated. If we look at Figure 3, we see that the maximum magnitudes, generated by the complete rupture of the Carboneras fault, vary roughly between magnitudes 6.9 and 7.7 (maximum absolute value of 7.62). If we use the empirical relationship of Leonard (2014) for example, for a maximum rupture length of 71 km (using the Gómez de la Peña et al. (2022) value) we obtain magnitudes of 7.25 and using the rupture area we obtain values of 7.14. However, these values represent the mean of the best fit, with a one standard deviation range between 6.86 and 7.64 for the empirical length- M_W relationship and between 6.88 and 7.4 for the area- M_W relationship. Therefore, the values obtained in our model are within the range of one standard deviation of this empirical relationship, with the advantage that we can obtain the maximum magnitudes in a robust manner from a statistical point of view.

The distribution of frequencies and magnitudes (FMD) of the generated seismic catalogue (Figure 3) reflects the variability of magnitudes associated to the rupture of the entire fault. Since the long-term behaviour of the modelled system is complex, although the construction of the model is deterministic, the statistical distribution of the generated events reflects the stochastic behaviour characteristic of dynamical systems showing self-organized criticality (SOC) (Bak et al., 1988; Bak and Tang, 1989). This stochastic behaviour of the system is reflected also in the non-linearity of the relationship between the size of the earthquake rupture and the slip; thus, for the same rupture size we obtain different slip distributions and therefore different magnitudes are generated. Maybe as a consequence of this, the upper limit of the FMD departs from the classical Gutenberg-Richter potential relation (GR), showing a distribution markedly different that can be seen on the discrete counts of the plot in Figure 3. This distribution resembles that of the characteristic earthquake behaviour (Schwartz and Coppersmith, 1984), but instead of showing a characteristic single magnitude there is a bell-shaped distribution of the characteristic earthquake magnitudes. In our models this behaviour can be related to the physical limit imposed to the maximum rupture area and consequently limiting the self-similar range of the dynamic system (Ben-Zion and Rice, 1995); maybe if the rupture area could be modelled as infinite, the FMD would reflect a GR relation.

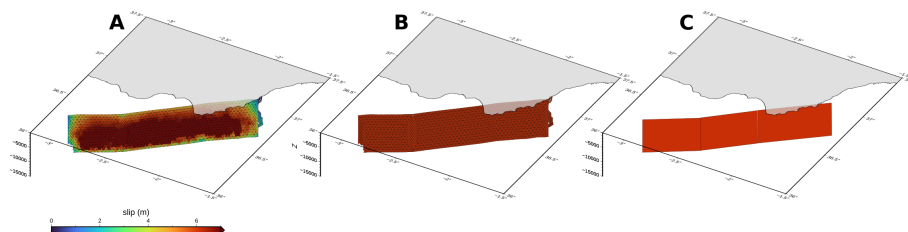


Figure 12. Comparison of source simplifications. a) Realistic geometry and variable slip maximum earthquake, M_W 7.62, model; b) realistic geometry with average homogeneous slip; c) simplified geometry and homogeneous slip.

Worst-case scenario approximation

280 This concept of characteristic earthquake, or worst-case scenario, is frequently used in deterministic hazard approximations. In these models, simple rectangular sources with homogeneous slips over the fault rupture are used. There has been much debate about the appropriateness of using these simple models and whether they can roughly reflect the tsunamigenic potential of a source. To address some of the drawbacks of this methodology, stochastic probabilistic approaches have been proposed for the generation of variable slips on the fault plane. In principle, the variable slip should play a key role on the impact of local

285 sources, which has been seen in the models shown in Figure 8 for events of different magnitudes (see supplementary models for comparison). To analyse the influence of these aspects we have compared one of the maximum scenarios modelled, with magnitude M_W 7.62 (Figure 12a), with scenarios of equal magnitude but with homogeneous slip in the detailed geometry (Figure 12b), as well as with a simplistic model based on 3 rectangular sections like the one used by Álvarez-Gómez et al. (2011a) (Figure 12c).

290 At first glance, the propagations are very similar and share their main features. If we compare them at a local scale (Figure 13), we see that the differences are below 0.5 m in general, although locally the differences may be greater on the coast (up to 3 m). From the regional point of view, the differences are minor (Figure 14).

If we compare the local propagation between the simplified rectangular source and the variable slip source (Figure 13d) the main differences are located towards the tips of the fault sections. These sections behave as patches whose slip decreases

295 towards the tips (Figure 12a), and it is therefore at these points where the simplified model overestimates sea-floor uplift (the blue colours in figure 13d show this important difference in the Adra area). On the contrary, towards the centre of the sections the simplified model underestimates the uplift. These differences are essentially the same as those that can be observed in the comparison of both realistic geometries but with variable or constant slips (Figure 13e). In this case, since both geometries are the same, the differences between both models are minor.

300 Regionally, the differences between the models are minor, although the slip differences towards the southern tip of the fault are evident, as has been seen locally as well. On both the Iberian and African coasts, values are overestimated by the simplified models towards the western part of the basin (negative values in Figures 14d and e), while elevations are underestimated towards the eastern part.

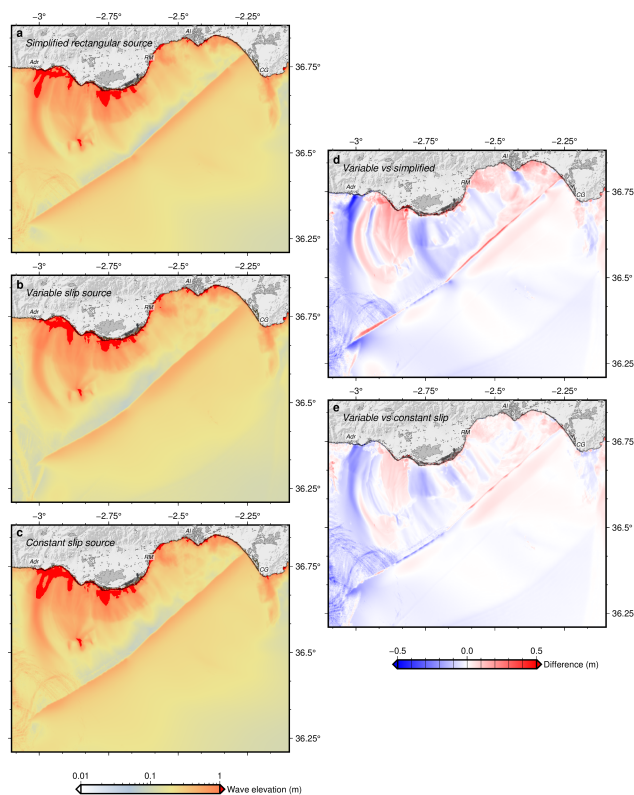


Figure 13. Comparison of local propagations for the simplified sources shown in Figure 12. a) Propagation of the simplified rectangular source. b) Propagation of the variable slip and realistic geometry source. c) Propagation of the homogeneous slip source with realistic geometry. d) Differences between variable and simplified sources. e) Differences between variable and constant slip sources. See Figure 7 for labels.

What is evident is the main role that bathymetry plays in the propagation features, determining to a large extent the location of the areas where there is major impact (Figure 9). In this sense, the Chella Bank, off the coast of Adra (Figure 7), determines the wave propagation and the impact on this coast, in which the highest wave elevations are observed (Figure 11).

5 Conclusions

From a deterministic point of view, the one adopted in this work, the use of physics-based earthquake simulations for tsunami-genic sources allows a more robust characterization of the scenarios, either through aggregated maps of maximum elevations (Figure 9) or the statistical exploitation of the hundreds or thousands of scenarios generated (Figure 11). In addition, the use of this tool allows characterizing the inter-event times and the recurrence intervals of the maximum events, which are those that have the greatest impact on the tsunami hazard.

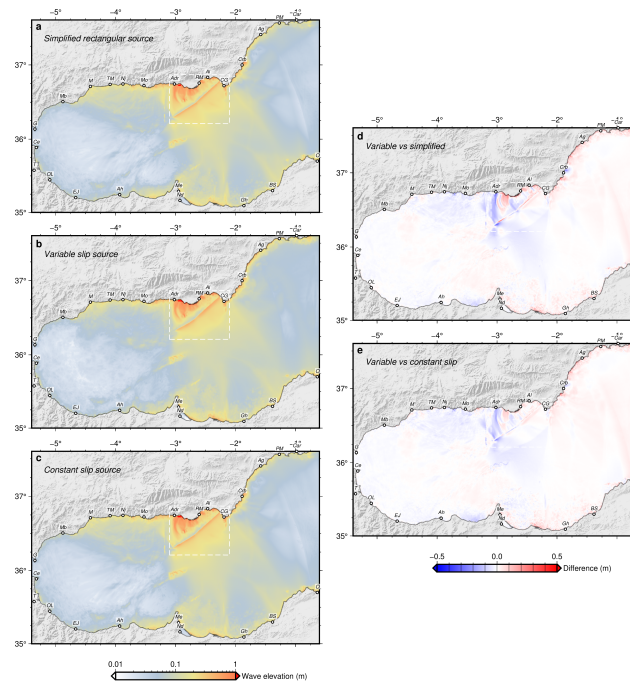


Figure 14. Comparison of regional propagations for the simplified sources shown in Figure 12. a) Propagation of the simplified rectangular source. b) Propagation of the variable slip and realistic geometry source. c) Propagation of the homogeneous slip source with realistic geometry. d) Differences between variable and simplified sources. e) Differences between variable and constant slip sources. See Figure 7 for labels.

Regarding the estimation of the maximum magnitude of a source, a key step in the deterministic characterization of the tsunami impact, this methodology incorporates the stochastic natural variation in rupture area, slip and magnitude that arises from the non-linear process of seismic rupture. Thus, instead of characterizing the size of the worst-case earthquake through empirical relationships, we can obtain a range of magnitudes characterized by a probability distribution, which allows a robust implementation of uncertainty estimation. In addition, each modelled seismic rupture is characterized by its own variable slip distribution and rupture process as they are modelled with a quasi-dynamic algorithm.

The strike-slip Carboneras Fault has the capacity to generate locally damaging tsunamis. However, on a regional scale, considering the Alboran Sea basin, its tsunamigenic capacity is more limited. Comparing our results with previous works (Álvarez-Gómez et al., 2011a, b; Gómez de la Peña et al., 2022) we can see that the tsunamigenic capacity modelled here is higher, basically due to the difference in maximum magnitude, which produces an important difference in maximum net slip.

The distribution of frequencies and magnitudes (FMD) of the generated seismic catalogue (Figure 3) reflects the variability of magnitudes associated to the rupture of the entire fault. The upper limit of the FMD departs from the classical Gutenberg-Richter potential relation, showing a bell-shaped distribution of the maximum earthquakes magnitude in a range between 6.9 and 7.7. The inter-event time for these magnitudes is around 2000 – 6000 years (Figure 4).



The use of physics-based earthquake simulations for tsunamigenic sources allows a qualitative leap in their characterization. From a probabilistic point of view, these models have shown in the Probabilistic Seismic Hazard Analyses (PSHA) a great potential to estimate recurrence periods and inter-event times for large earthquakes, which are poorly represented in the instrumental seismic catalogues (Chartier et al., 2021; Herrero-Barbero et al., 2021; Console et al., 2017); being one of the key pieces in the current development of seismic forecast models (Dieterich and Richards-Dinger, 2010; Field, 2019; Field et al., 2014; Shaw et al., 2018). The implementation of these methodologies in the Probabilistic Tsunami Hazard Analyses (PTHA) is a logical and necessary step.

Code availability. The RSQSim physics-based earthquake simulator has been developed by Richards-Dinger and Dieterich (2012) and can be obtained from the authors upon request. The COMCOT tsunami simulation has been developed by Liu et al. (1995). The version used in this work is an adaptation to gfortran compiler developed by Tao, Chiu at Tsunami research group, IHOS, NCU; available at <https://github.com/AndybnACT/comcot-gfortran>. GMT (Wessel et al., 2013) has been used to perform some calculations and to produce most of the figures.

Author contributions. JAAG conceived the work, performed the tsunami simulations and analysis and collaborated on the manuscript writing. PHB constructed the 3D fault model, performed the physics-based earthquake simulations and analysis and collaborated on the manuscript writing. JJMD collaborated on the manuscript writing and on the discussions on the EBSZ tectonics.

Competing interests. The authors declare no competing interests.

Acknowledgements. The bathymetry used has been provided by the EMODnet Bathymetry Consortium (EMODnet, 2022). This work has been partially funded by the project SHaKER (PID2021-124155NB-C31) of the Spanish National Research Agency.



345 References

- Álvarez-Gómez, J. A., Aniel-Quiroga, Í., González, M., Olabarrieta, M., and Carreño, E.: Scenarios for earthquake-generated tsunamis on a complex tectonic area of diffuse deformation and low velocity: The Alboran Sea, Western Mediterranean, *Marine Geology*, 284, 55–73, publisher: Elsevier, 2011a.
- Álvarez-Gómez, J. A., Aniel-Quiroga, Í., González, M., and Otero, L.: Tsunami hazard at the Western Mediterranean Spanish coast from
 350 seismic sources, *Nat. Hazards Earth Syst. Sci.*, 11, 227–240, 2011b.
- Bak, P. and Tang, C.: Earthquakes as a self-organized critical phenomenon, *Journal of Geophysical Research*, 94, 15 635–15 637, 1989.
- Bak, P., Tang, C., and Wiesenfeld, K.: Self-organized criticality, *Physical Review A*, 38, 364–374, <https://doi.org/10.1103/PhysRevA.38.364>, 1988.
- Ballesteros, M., Rivera, J., noz, A. M., noz Martín, A. M., Acosta, J., Carbó, A., and Uchupi, E.: Alboran Basin, southern Spain—Part II:
 355 Neogene tectonic implications for the orogenic float model, *Marine and Petroleum Geology*, 25, 75–101, 2008.
- Ben-Zion, Y. and Rice, J. R.: Slip patterns and earthquake populations along different classes of faults in elastic solids, *Journal of Geophysical Research: Solid Earth*, 100, 12 959–12 983, <https://doi.org/10.1029/94JB03037>, 1995.
- Bolshakova, A. V. and Nosov, M. A.: Parameters of Tsunami Source Versus Earthquake Magnitude, *Pure and Applied Geophysics*, 168, 2023–2031, <https://doi.org/10.1007/s00024-011-0285-3>, 2011.
- Borghini, M., Bryden, H., Schroeder, K., Sparnocchia, S., and Vetrano, A.: The Mediterranean is becoming saltier, *Ocean Science*, 10, 693–700, <https://doi.org/10.5194/os-10-693-2014>, 2014.
- Borque, M. J., Sánchez-Alzola, A., Martín-Rojas, I., Alfaro, P., Molina, S., Rosa-Cintas, S., Rodríguez-Caderot, G., de Lacy, C., García-Armenteros, J. A., Avilés, M., Herrera-Olmo, A., García-Tortosa, F. J., Estévez, A., and Gil, A. J.: How Much Nubia-Eurasia Convergence Is Accommodated by the NE End of the Eastern Betic Shear Zone (SE Spain)? Constraints From GPS Velocities, *Tectonics*, 38, 1824–
 365 1839, <https://doi.org/10.1029/2018TC004970>, 2019.
- Bourgeois, J., Mauffret, A., Ammar, N. A., and Demnati, N. A.: Multichannel seismic data imaging of inversion tectonics of the Alboran Ridge (Western Mediterranean Sea), *Geo-Marine Letters*, 12, 117–122, 1992.
- Bousquet, J.-C.: Quaternary strike-slip faults in southeastern Spain, *Tectonophysics*, 52, 277–286, [https://doi.org/10.1016/0040-1951\(79\)90232-4](https://doi.org/10.1016/0040-1951(79)90232-4), 1979.
- Burbidge, D., Mueller, C., and Power, W.: The effect of uncertainty in earthquake fault parameters on the maximum wave height from a tsunami propagation model, *Natural Hazards and Earth System Sciences*, 15, 2299–2312, <https://doi.org/10.5194/nhess-15-2299-2015>, 2015.
- Chartier, T., Scotti, O., Lyon-Caen, H., Richard-Dinger, K., Dieterich, J. H., and Shaw, B. E.: Modelling earthquake rates and associated uncertainties in the Marmara Region, Turkey, *Natural Hazards and Earth System Sciences*, 21, 2733–2751, <https://doi.org/10.5194/nhess-21-2733-2021>, 2021.
- Chertova, M. V., Spakman, W., Geenen, T., van den Berg, A. P., and van Hinsbergen, D. J. J.: Underpinning tectonic reconstructions of the western Mediterranean region with dynamic slab evolution from 3-D numerical modeling, *Journal of Geophysical Research: Solid Earth*, 119, 5876–5902, <https://doi.org/10.1002/2014JB011150>, 2014.
- CNIG, Centro Nacional de Información Geográfica: Modelo Digital del Terreno - MDT25, <http://centrodedescargas.cnig.es>, 2022.
- 380 Comas, M. C., Dueñas, V. G., and Jurado, M. J.: Neogene tectonic evolution of the Alboran Basin from MCS data, *Geo-Marine Letters*, 12, 157–164, 1992.



- Console, R., Carluccio, R., Papadimitriou, E., and Karakostas, V.: Synthetic earthquake catalogs simulating seismic activity in the Corinth Gulf, Greece, fault system, *Journal of Geophysical Research: Solid Earth*, 120, 326–343, <https://doi.org/10.1002/2014JB011765>, 2015.
- 385 Console, R., Nardi, A., Carluccio, R., Murru, M., Falcone, G., and Parsons, T.: A physics-based earthquake simulator and its application to seismic hazard assessment in Calabria (Southern Italy) region, *Acta Geophysica*, 65, 243–257, <https://doi.org/10.1007/s11600-017-0020-2>, 2017.
- Console, R., Vannoli, P., and Carluccio, R.: The seismicity of the Central Apennines (Italy) studied by means of a physics-based earthquake simulator, *Geophysical Journal International*, 212, 916–929, <https://doi.org/10.1093/gji/ggx451>, 2018.
- 390 Dieterich, J. H.: Modeling of rock friction: 1. Experimental results and constitutive equations, *Journal of Geophysical Research: Solid Earth*, 84, 2161–2168, <https://doi.org/10.1029/JB084iB05p02161>, 1979.
- Dieterich, J. H.: Earthquake nucleation on faults with **rate-and state-dependent** strength, *Tectonophysics*, 211, 115–134, [https://doi.org/10.1016/0040-1951\(92\)90055-B](https://doi.org/10.1016/0040-1951(92)90055-B), 1992.
- Dieterich, J. H.: Earthquake simulations with time-dependent nucleation and long-range interactions, *Nonlinear Processes in Geophysics*, 2, 109–120, 1995.
- 395 Dieterich, J. H. and Richards-Dinger, K. B.: Earthquake Recurrence in Simulated Fault Systems, in: *Seismogenesis and Earthquake Forecasting: The Frank Evison Volume II*, edited by Savage, M. K., Rhoades, D. A., Smith, E. G. C., Gerstenberger, M. C., and Vere-Jones, D., pp. 233–250, Springer, Basel, https://doi.org/10.1007/978-3-0346-0500-7_15, 2010.
- Do Couto, D., Gorini, C., Jolivet, L., Lebreton, N., Augier, R., Gumiaux, C., d’Acremont, E., Ammar, A., Jabour, H., and Auxietre, J.-L.: Tectonic and stratigraphic evolution of the Western Alboran Sea Basin in the last 25Myrs, *Tectonophysics*, 677–678, 280–311, <https://doi.org/10.1016/j.tecto.2016.03.020>, 2016.
- 400 Dotsenko, S. F. and Soloviev, S. L.: Mathematical modeling of tsunami excitation process by displacement of the ocean bottom, *Tsunami researches (in Russian)*, 4, 8–20, 1990.
- Echeverria, A., Khazaradze, G., Asensio, E., Gárate, J., Dávila, J. M., and Suriñach, E.: Crustal deformation in eastern Betics from CuaTeNeo GPS network, *Tectonophysics*, 608, 600–612, <https://doi.org/10.1016/j.tecto.2013.08.020>, 2013.
- 405 Echeverria, A., Khazaradze, G., Asensio, E., and Masana, E.: Geodetic evidence for continuing tectonic activity of the Carboneras fault (SE Spain), *Tectonophysics*, 663, 302–309, <https://doi.org/10.1016/j.tecto.2015.08.009>, 2015.
- Elbanna, A., Abdelmeguid, M., Ma, X., Amlani, F., Bhat, H. S., Synolakis, C., and Rosakis, A. J.: Anatomy of strike-slip fault tsunami genesis, *Proceedings of the National Academy of Sciences*, 118, <https://doi.org/10.1073/pnas.2025632118>, 2021.
- EMODnet: EMODnet Digital Bathymetry (DTM 2020), 2022.
- 410 Faccenna, C., Piromallo, C., Crespo-Blanc, A., Jolivet, L., and Rossetti, F.: Lateral slab deformation and the origin of the western Mediterranean arcs, *Tectonics*, 23, TC1012, [doi:10.1029/2002TC001488](https://doi.org/10.1029/2002TC001488), 2004.
- Faulkner, D. R., Lewis, A. C., and Rutter, E. H.: On the internal structure and mechanics of large strike-slip fault zones: field observations of the Carboneras fault in southeastern Spain, *Tectonophysics*, 367, 235–251, [https://doi.org/10.1016/S0040-1951\(03\)00134-3](https://doi.org/10.1016/S0040-1951(03)00134-3), 2003.
- Field, E. H.: How Physics-Based Earthquake Simulators Might Help Improve Earthquake Forecasts, *Seismological Research Letters*, 90, <https://doi.org/10.1785/0220180299>, 2019.
- 415 Field, E. H., Arrowsmith, R. J., Biasi, G. P., Bird, P., Dawson, T. E., Felzer, K. R., Jackson, D. D., Johnson, K. M., Jordan, T. H., Madden, C., Michael, A. J., Milner, K. R., Page, M. T., Parsons, T., Powers, P. M., Shaw, B. E., Thatcher, W. R., Weldon, II, R. J., and Zeng, Y.: Uniform California Earthquake Rupture Forecast, Version 3 (UCERF3)—The Time-Independent Model, *Bulletin of the Seismological Society of America*, 104, 1122–1180, <https://doi.org/10.1785/0120130164>, 2014.



- 420 Frucht, E., Salamon, A., Gal, E., Ginat, H., Grigorovitch, M., Shem Tov, R., and Ward, S.: A Fresh View of the Tsunami Generated by the
 Dead Sea Transform, 1995 Mw 7.2 Nuweiba Earthquake, along the Gulf of Elat–Aqaba, *Seismological Research Letters*, 90, 1483–1493,
<https://doi.org/10.1785/0220190004>, 2019.
- Fujii, Y., Satake, K., Sakai, S., Shinohara, M., and Kanazawa, T.: Tsunami source of the 2011 off the Pacific coast of Tohoku Earthquake,
Earth, Planets and Space, 63, 55, <https://doi.org/10.5047/eps.2011.06.010>, 2011.
- 425 García-Mayordomo, J., Martín-Banda, R., Insua-Arévalo, J. M., Álvarez-Gómez, J. A., Martínez-Díaz, J. J., and Cabral, J.: Active fault
 databases: building a bridge between earthquake geologists and seismic hazard practitioners, the case of the QAFI v.3 database, *Natural
 Hazards and Earth System Sciences*, 17, 1447–1459, <https://doi.org/10.5194/nhess-17-1447-2017>, 2017.
- Geist, E. L.: Local Tsunamis and Earthquake Source Parameters, in: *Advances in Geophysics*, edited by Dmowska, R. and Saltzman, B.,
 vol. 39 of *Tsunamigenic Earthquakes and Their Consequences*, pp. 117–209, Elsevier, [https://doi.org/10.1016/S0065-2687\(08\)60276-9](https://doi.org/10.1016/S0065-2687(08)60276-9),
 430 1998.
- Geist, E. L.: Complex earthquake rupture and local tsunamis, *Journal of Geophysical Research: Solid Earth*, 107, ESE 2–1–ESE 2–15,
<https://doi.org/10.1029/2000JB000139>, 2002.
- Gibbons, S. J., Lorito, S., de la Asunción, M., Volpe, M., Selva, J., Macías, J., Sánchez-Linares, C., Brizuela, B., Vöge, M., Tonini, R.,
 Lanucara, P., Glimsdal, S., Romano, F., Meyer, J. C., and Løvholt, F.: The Sensitivity of Tsunami Impact to Earthquake Source Parameters
 435 and Manning Friction in High-Resolution Inundation Simulations, *Frontiers in Earth Science*, 9, 2022.
- Gimbutas, Z., Greengard, L., Barall, M., and Tullis, T. E.: On the Calculation of Displacement, Stress, and Strain Induced by Triangular
 Dislocations, *Bulletin of the Seismological Society of America*, 102, 2776–2780, <https://doi.org/10.1785/0120120127>, 2012.
- Goda, K., Yasuda, T., Mori, N., and Mai, P. M.: Variability of tsunami inundation footprints considering stochastic scenarios based
 on a single rupture model: Application to the 2011 Tohoku earthquake, *Journal of Geophysical Research: Oceans*, 120, 4552–4575,
 440 <https://doi.org/10.1002/2014JC010626>, 2015.
- Gómez de la Peña, L., R. Ranero, C., Gràcia, E., and Booth-Rea, G.: The evolution of the westernmost Mediterranean basins, *Earth-Science
 Reviews*, 214, 103 445, <https://doi.org/10.1016/j.earscirev.2020.103445>, 2021.
- Gómez de la Peña, L., Gràcia, E., Maesano, F. E., Basili, R., Kopp, H., Sánchez-Serra, C., Scala, A., Romano, F., Volpe, M., Piatanesi,
 A., and R. Ranero, C.: A first appraisal of the seismogenic and tsunamigenic potential of the largest fault systems in the westernmost
 445 Mediterranean, *Marine Geology*, 445, 106 749, <https://doi.org/10.1016/j.margeo.2022.106749>, 2022.
- Gràcia, E., Pallàs, R., Soto, J. I., Comas, M., Moreno, X., Masana, E., Santanach, P., Diez, E., García, M., and Dañobeitia, J.: Active faulting
 offshore SE Spain (Alboran Sea): Implications for earthquake hazard assessment in the Southern Iberian Margin, *Earth and Planetary
 Science Letters*, 241, 734–749, 2006.
- Gusiakov, V. K.: Relationship of Tsunami Intensity to Source Earthquake Magnitude as Retrieved from Historical Data, *Pure and Applied
 450 Geophysics*, 168, 2033–2041, <https://doi.org/10.1007/s00024-011-0286-2>, 2011.
- Gusman, A. R., Tanioka, Y., Sakai, S., and Tsushima, H.: Source model of the great 2011 Tohoku earthquake estimated from tsunami wave-
 forms and crustal deformation data, *Earth and Planetary Science Letters*, 341–344, 234–242, <https://doi.org/10.1016/j.epsl.2012.06.006>,
 2012.
- Gusman, A. R., Satake, K., and Harada, T.: Rupture process of the 2016 Wharton Basin strike-slip faulting earthquake estimated from joint
 455 inversion of teleseismic and tsunami waveforms, *Geophysical Research Letters*, 44, 4082–4089, <https://doi.org/10.1002/2017GL073611>,
 2017.



- Harris, R. A., Barall, M., Aagaard, B., Ma, S., Roten, D., Olsen, K., Duan, B., Liu, D., Luo, B., Bai, K., Ampuero, J.-P., Kaneko, Y., Gabriel, A.-A., Duru, K., Ulrich, T., Wollherr, S., Shi, Z., Dunham, E., Bydlon, S., Zhang, Z., Chen, X., Somala, S. N., Pelties, C., Tago, J., Cruz-Atienza, V. M., Kozdon, J., Daub, E., Aslam, K., Kase, Y., Withers, K., and Dalguer, L.: A Suite of Exercises for Verifying Dynamic Earthquake Rupture Codes, *Seismological Research Letters*, 89, 1146–1162, <https://doi.org/10.1785/0220170222>, 2018.
- Heidarzadeh, M., Harada, T., Satake, K., Ishibe, T., and Takagawa, T.: Tsunamis from strike-slip earthquakes in the Wharton Basin, northeast Indian Ocean: March 2016 Mw7.8 event and its relationship with the April 2012 Mw 8.6 event, *Geophysical Journal International*, 211, 1601–1612, <https://doi.org/10.1093/gji/ggx395>, 2017.
- Herrero-Barbero, P., Alvarez-Gomez, J. A., Martinez-Diaz, J. J., and Klimowitz, J.: Neogene Basin Inversion and Recent Slip Rate Distribution of the Northern Termination of the Alhama de Murcia Fault (Eastern Betic Shear Zone, SE Spain), *Tectonics*, 39, e2019TC005750, <https://doi.org/10.1029/2019TC005750>, 2020.
- Herrero-Barbero, P., Álvarez-Gómez, J. A., Williams, C., Villamor, P., Insua-Arévalo, J. M., Alonso-Henar, J., and Martínez-Díaz, J. J.: Physics-Based Earthquake Simulations in Slow-Moving Faults: A Case Study From the Eastern Betic Shear Zone (SE Iberian Peninsula), *Journal of Geophysical Research: Solid Earth*, 126, e2020JB021133, <https://doi.org/10.1029/2020JB021133>, 2021.
- Ho, T.-C., Satake, K., Watada, S., Hsieh, M.-C., Chuang, R. Y., Aoki, Y., Mulia, I. E., Gusman, A. R., and Lu, C.-H.: Tsunami Induced by the Strike-Slip Fault of the 2018 Palu Earthquake (Mw = 7.5), Sulawesi Island, Indonesia, *Earth and Space Science*, 8, <https://doi.org/http://dx.doi.org/10.1029/2020EA001400>, 2021.
- Hornbach, M. J., Braudy, N., Briggs, R. W., Cormier, M.-h., Davis, M. B., Diebold, J. B., Dieudonne, N., Douilly, R., Frohlich, C., Gulick, S. P. S., Johnson Iii, H. E., Mann, P., Mchugh, C., Ryan-mishkin, K., Prentice, C. S., Seeber, L., Sorlien, C. C., Steckler, M. S., Symithe, S. J., Taylor, F. W., and Templeton, J.: High tsunami frequency as a result of combined strike-slip faulting and coastal landslides, *Nature Geoscience*, 3, 783–788, <https://doi.org/http://dx.doi.org/10.1038/ngeo975>, 2010.
- Howarth, J. D., Barth, N. C., Fitzsimons, S. J., Richards-Dinger, K., Clark, K. J., Biasi, G. P., Cochran, U. A., Langridge, R. M., Berryman, K. R., and Sutherland, R.: Spatiotemporal clustering of great earthquakes on a transform fault controlled by geometry, *Nature Geoscience*, 14, 314–320, <https://doi.org/10.1038/s41561-021-00721-4>, 2021.
- IGN-UPM: Actualización de mapas de peligrosidad sísmica de España 2012., vol. 267, 2013.
- Kozdon, J. E. and Dunham, E. M.: Rupture to the Trench: Dynamic Rupture Simulations of the 11 March 2011 Tohoku Earthquake, *Bulletin of the Seismological Society of America*, 103, 1275–1289, <https://doi.org/10.1785/0120120136>, 2013.
- Lavallée, D., Liu, P., and Archuleta, R. J.: Stochastic model of heterogeneity in earthquake slip spatial distributions, *Geophysical Journal International*, 165, 622–640, <https://doi.org/10.1111/j.1365-246X.2006.02943.x>, 2006.
- Legg, M., Borrero, J., and Synolakis, C.: Tsunami Hazards From Strike-Slip Earthquakes, AGU Fall Meeting Abstracts, 2003.
- Leonard, M.: Self-Consistent Earthquake Fault-Scaling Relations: Update and Extension to Stable Continental Strike-Slip Faults, *Bulletin of the Seismological Society of America*, 104, 2953–2965, <https://doi.org/10.1785/0120140087>, 2014.
- Liu, P. L. F., Cho, Y. S., Yoon, S. B., and Seo, S. N.: Numerical Simulations of the 1960 Chilean Tsunami Propagation and Inundation at Hilo, Hawaii, in: *Tsunami: Progress in Prediction, Disaster Prevention and Warning*, edited by Tsuchiya, Y. and Shuto, N., *Advances in Natural and Technological Hazards Research*, pp. 99–115, Springer Netherlands, Dordrecht, https://doi.org/10.1007/978-94-015-8565-1_7, 1995.
- Løvholt, F., Pedersen, G., Bazin, S., Kühn, D., Bredesen, R. E., and Harbitz, C.: Stochastic analysis of tsunami runup due to heterogeneous coseismic slip and dispersion, *Journal of Geophysical Research: Oceans*, 117, <https://doi.org/10.1029/2011JC007616>, 2012.



- Madden, E. H., Bader, M., Behrens, J., van Dinther, Y., Gabriel, A.-A., Rannabauer, L., Ulrich, T., Uphoff, C., Vater, S., and van Zelst, I.: Linked 3-D modelling of megathrust earthquake-tsunami events: from subduction to tsunami run up, *Geophysical Journal International*, 224, 487–516, <https://doi.org/10.1093/gji/ggaa484>, 2021.
- Maeda, T. and Furumura, T.: FDM Simulation of Seismic Waves, Ocean Acoustic Waves, and Tsunamis Based on Tsunami-Coupled Equations of Motion, *Pure and Applied Geophysics*, 170, 109–127, <https://doi.org/10.1007/s00024-011-0430-z>, 2013.
- Mai, P. M. and Beroza, G. C.: A spatial random field model to characterize complexity in earthquake slip, *Journal of Geophysical Research: Solid Earth*, 107, ESE 10–1–ESE 10–21, <https://doi.org/10.1029/2001JB000588>, 2002.
- Mansinha, L. and Smylie, D. E.: The displacement fields of inclined faults, *Bulletin of the Seismological Society of America*, 61, 1433–1440, 1971.
- Martínez-García, P.: Recent tectonic evolution of the Alboran Ridge and Yusuf regions, Ph.D. thesis, Universidad de Granada, 2012.
- Martínez-García, P., Comas, M., Soto, J. I., Lonergan, L., and Watts, A. B.: Strike-slip tectonics and basin inversion in the Western Mediterranean: the Post-Messinian evolution of the Alboran Sea, *Basin Research*, 25, 361–387, <https://doi.org/10.1111/bre.12005>, 2013.
- Martínez-García, P., Comas, M., Lonergan, L., and Watts, A. B.: From Extension to Shortening: Tectonic Inversion Distributed in Time and Space in the Alboran Sea, Western Mediterranean, *Tectonics*, 36, 2777–2805, <https://doi.org/10.1002/2017TC004489>, 2017.
- Martínez Solares, J. M. and Mezcua, J.: Catálogo sísmico de la Península Ibérica:(880 a. C-1900), Ministerio de Fomento, 2002.
- Masana, E., Moreno, X., Gràcia, E., Pallàs, R., Ortuño, M., López, R., Gómez-Novell, O., Ruano, P., Perea, H., Stepancikova, P., and Khazaradze, G.: First evidence of paleoearthquakes along the Carboneras Fault Zone (SE Iberian Peninsula): Los Trances site, *Geologica Acta*, pp. 461–476, 2018.
- McCloskey, J., Antonioli, A., Piatanesi, A., Sieh, K., Steacy, S., Nalbant, S., Cocco, M., Giunchi, C., Huang, J., and Dunlop, P.: Tsunami threat in the Indian Ocean from a future megathrust earthquake west of Sumatra, *Earth and Planetary Science Letters*, 265, 61–81, <https://doi.org/10.1016/j.epsl.2007.09.034>, 2008.
- Meade, B. J.: Algorithms for the calculation of exact displacements, strains, and stresses for triangular dislocation elements in a uniform elastic half space, *Computers & Geosciences*, 33, 1064–1075, <https://doi.org/10.1016/j.cageo.2006.12.003>, 2007.
- Moreno, X.: Neotectonic and Paleoseismic Onshore-Offshore integrated study of the Carboneras Fault (Eastern Betics, SE Iberia) / Estudio integrado tierra-mar de la Neotectónica y Paleosismología de la Falla de Carboneras (Béticas Orientales, SE Península Ibérica), Ph.D. Thesis, Universitat de Barcelona, 2011.
- Moreno, X., Masana, E., Pallàs, R., Gràcia, E., Rodés, Á., and Bordonau, J.: Quaternary tectonic activity of the Carboneras Fault in the La Serrata range (SE Iberia): Geomorphological and chronological constraints, *Tectonophysics*, 663, 78–94, <https://doi.org/10.1016/j.tecto.2015.08.016>, 2015.
- National Geophysical Data Center: Global Historical Tsunami Database, <https://doi.org/10.7289/V5PN93H7>, type: dataset, 2022.
- Niemeijer, A. R. and Vissers, R. L. M.: Earthquake rupture propagation inferred from the spatial distribution of fault rock frictional properties, *Earth and Planetary Science Letters*, 396, 154–164, <https://doi.org/10.1016/j.epsl.2014.04.010>, 2014.
- Nikkhoo, M. and Walter, T. R.: Triangular dislocation: an analytical, artefact-free solution, *Geophysical Journal International*, 201, 1119–1141, <https://doi.org/10.1093/gji/ggv035>, 2015.
- Noda, H. and Lapusta, N.: Stable creeping fault segments can become destructive as a result of dynamic weakening, *Nature*, 493, 518–521, <https://doi.org/10.1038/nature11703>, 2013.
- Nosov, M. A., Bolshakova, A. V., and Kolesov, S. V.: Displaced Water Volume, Potential Energy of Initial Elevation, and Tsunami Intensity: Analysis of Recent Tsunami Events, *Pure and Applied Geophysics*, 171, 3515–3525, <https://doi.org/10.1007/s00024-013-0730-6>, 2014.



- Okada, Y.: Surface deformation due to shear and tensile faults in a half-space, *Bulletin of the Seismological Society of America*, 75, 1135–1154, 1985.
- Okada, Y.: Internal deformation due to shear and tensile faults in a half-space, *Bulletin of the Seismological Society of America*, 82, 1018–1040, 1992.
- 535 Pollitz, F. F.: ViscoSim Earthquake Simulator, *Seismological Research Letters*, 83, 979–982, <https://doi.org/10.1785/0220120050>, 2012.
- Reicherter, K. and Becker-Heidmann, P.: Tsunami deposits in the western Mediterranean: Remains of the 1522 Almería earthquake?, *Geological Society Special Publication*, 316, 217–235, <https://doi.org/10.1144/SP316.14>, 2009.
- Reicherter, K. and Hübscher, C.: Evidence for a seafloor rupture of the Carboneras Fault Zone (southern Spain): Relation to the 1522 Almería earthquake?, *Journal of Seismology*, 11, 15–26, <https://doi.org/10.1007/s10950-006-9024-0>, 2007.
- 540 Richards-Dinger, K. and Dieterich, J. H.: RSQSim Earthquake Simulator, *Seismological Research Letters*, 83, 983–990, <https://doi.org/10.1785/0220120105>, 2012.
- Robinson, R. and Benites, R.: Synthetic seismicity models of multiple interacting faults, *Journal of Geophysical Research: Solid Earth*, 100, 18 229–18 238, <https://doi.org/10.1029/95JB01569>, 1995.
- Robinson, R., Van Dissen, R., and Litchfield, N.: Using synthetic seismicity to evaluate seismic hazard in the Wellington region, New Zealand, *Geophysical Journal International*, 187, 510–528, <https://doi.org/10.1111/j.1365-246X.2011.05161.x>, 2011.
- 545 Rodríguez Escudero, E.: Implicaciones de la estructura interna de una zona de falla activa en la génesis de terremotos, Ph.D. Thesis, Universidad Autónoma de Madrid, 2017.
- Romagny, A., Jolivet, L., Menant, A., Bessi re, E., Maillard, A., Canva, A., Gorini, C., and Augier, R.: Detailed tectonic reconstructions of the Western Mediterranean region for the last 35 Ma, insights on driving mechanisms, *Bulletin de la Soci t  G ologique de France*, 191, <https://doi.org/http://dx.doi.org/10.1051/bsgf/2020040>, 2020.
- 550 Rosenbaum, G. and Lister, G. S.: Formation of arcuate orogenic belts in the western Mediterranean region, *Orogenic curvature: integrating paleomagnetic and structural analyses*, 383, 41–56, 2004.
- Ruina, A.: Slip instability and state variable friction laws, *Journal of Geophysical Research: Solid Earth*, 88, 10 359–10 370, <https://doi.org/10.1029/JB088iB12p10359>, 1983.
- 555 Rundle, J. B.: A physical model for earthquakes: 2. Application to southern California, *Journal of Geophysical Research: Solid Earth*, 93, 6255–6274, <https://doi.org/10.1029/JB093iB06p06255>, 1988.
- Rutter, E. H., Faulkner, D. R., and Burgess, R.: Structure and geological history of the Carboneras Fault Zone, SE Spain: Part of a stretching transform fault system, *Journal of Structural Geology*, 45, 68–86, <https://doi.org/10.1016/j.jsg.2012.08.009>, 2012.
- Ryan, K. J., Geist, E. L., Barall, M., and Oglesby, D. D.: Dynamic models of an earthquake and tsunami offshore Ventura, California, *Geophysical Research Letters*, 42, 6599–6606, <https://doi.org/10.1002/2015GL064507>, 2015.
- 560 Sachs, M. K., Heien, E. M., Turcotte, D. L., Yikilmaz, M. B., Rundle, J. B., and Kellogg, L. H.: Virtual California Earthquake Simulator, *Seismological Research Letters*, 83, 973–978, <https://doi.org/10.1785/0220120052>, 2012.
- Satake, K., Fujii, Y., Harada, T., and Namegaya, Y.: Time and Space Distribution of Coseismic Slip of the 2011 Tohoku Earthquake as Inferred from Tsunami Waveform Data, *Bulletin of the Seismological Society of America*, 103, 1473–1492, <https://doi.org/10.1785/0120120122>, 2013.
- 565 Scholz, C. H.: Earthquakes and friction laws, *Nature*, 391, 37–42, <https://doi.org/10.1038/34097>, 1998.
- Schultz, K. W., Yoder, M. R., Wilson, J. M., Heien, E. M., Sachs, M. K., Rundle, J. B., and Turcotte, D. L.: Parametrizing Physics-Based Earthquake Simulations, in: *Earthquakes and Multi-hazards Around the Pacific Rim, Vol. I*, edited by Zhang, Y., Goebel, T., Peng, Z.,



- Williams, C. A., Yoder, M., and Rundle, J. B., pp. 75–84, Springer International Publishing, Cham, https://doi.org/10.1007/978-3-319-71565-0_6, 2018.
- Schwartz, D. P. and Coppersmith, J.: Fault behavior and characteristic earthquakes: Examples from the Wasatch and San Andreas fault zones, *Journal of Geophysical Research*, 89, 5681–5698, 1984.
- Serpelloni, E., Vannucci, G., Pondrelli, S., Argnani, A., Casula, G., Anzidei, M., Baldi, P., and Gasperini, P.: Kinematics of the Western Africa-Eurasia plate boundary from focal mechanisms and GPS data, *Geophysical Journal International*, 169, 1180–1200, <https://doi.org/10.1111/j.1365-246X.2007.03367.x>, 2007.
- Shaw, B. E., Milner, K. R., Field, E. H., Richards-Dinger, K., Gilchrist, J. J., Dieterich, J. H., and Jordan, T. H.: A physics-based earthquake simulator replicates seismic hazard statistics across California, *Science Advances*, 4(8), <https://doi.org/10.1126/sciadv.aau0688>, 2018.
- Somoza, L., Medialdea, T., Terrinha, P., Ramos, A., and Vázquez, J.-T.: Submarine Active Faults and Morpho-Tectonics Around the Iberian Margins: Seismic and Tsunamis Hazards, *Frontiers in Earth Science*, 9, 2021.
- Tanioka, Y. and Satake, K.: Tsunami generation by horizontal displacement of ocean bottom, *Geophysical Research Letters*, 23, 861–864, <https://doi.org/10.1029/96GL00736>, 1996.
- Tullis, T. E., Richards-Dinger, K., Barall, M., Dieterich, J. H., Field, E. H., Heien, E. M., Kellogg, L. H., Pollitz, F. F., Rundle, J. B., Sachs, M. K., Turcotte, D. L., Ward, S. N., and Burak Yikilmaz, M.: A Comparison among Observations and Earthquake Simulator Results for the allcal2 California Fault Model, *Seismological Research Letters*, 83, 994–1006, <https://doi.org/10.1785/0220120094>, 2012.
- Ulrich, T., Vater, S., Madden, E. H., Behrens, J., van Dinther, Y., van Zelst, I., Fielding, E. J., Liang, C., and Gabriel, A.-A.: Coupled, Physics-Based Modeling Reveals Earthquake Displacements are Critical to the 2018 Palu, Sulawesi Tsunami, *Pure and Applied Geophysics*, 176, 4069–4109, <https://doi.org/10.1007/s00024-019-02290-5>, 2019.
- Vernant, P., Fadil, A., Mourabit, T., Ouazar, D., Koulali, A., Davila, J. M., Garate, J., McClusky, S., and Reilinger, R.: Geodetic constraints on active tectonics of the Western Mediterranean: Implications for the kinematics and dynamics of the Nubia-Eurasia plate boundary zone, *Journal of Geodynamics*, 49, 123–129, <https://doi.org/10.1016/j.jog.2009.10.007>, 2010.
- Wang, X. and Liu, P. L.-F.: An analysis of 2004 Sumatra earthquake fault plane mechanisms and Indian Ocean tsunami, *Journal of Hydraulic Research*, 44, 147–154, 2006.
- Ward, S. N.: San Francisco Bay Area Earthquake Simulations: A Step Toward a Standard Physical Earthquake Model, *Bulletin of the Seismological Society of America*, 90, 370–386, <https://doi.org/10.1785/0119990026>, 2000.
- Ward, S. N.: ALLCAL Earthquake Simulator, *Seismological Research Letters*, 83, 964–972, <https://doi.org/10.1785/0220120056>, 2012.
- Wendt, J., Oglesby, D. D., and Geist, E. L.: Tsunamis and splay fault dynamics, *Geophysical Research Letters*, 36, <https://doi.org/10.1029/2009GL038295>, 2009.
- Wessel, P.: An Empirical Method for Optimal Robust Regional-Residual Separation of Geophysical Data, *Mathematical Geology*, 30, 391–408, <https://doi.org/10.1023/A:1021744224009>, 1998.
- Wessel, P., Smith, W. H. F., Scharroo, R., Luis, J., and Wobbe, F.: Generic Mapping Tools: Improved Version Released, *Eos, Transactions American Geophysical Union*, 94, 409–410, <https://doi.org/10.1002/2013EO450001>, 2013.
- Whirley, R. G. and Engelmann, B. E.: DYNA3D: A nonlinear, explicit, three-dimensional finite element code for solid and structural mechanics, User manual. Revision 1, Tech. Rep. UCRL-MA-107254-Rev.1, Lawrence Livermore National Lab., CA (United States), <https://doi.org/10.2172/10139227>, 1993.
- Wilson, A. and Ma, S.: Wedge Plasticity and Fully Coupled Simulations of Dynamic Rupture and Tsunami in the Cascadia Subduction Zone, *Journal of Geophysical Research: Solid Earth*, 126, e2020JB021627, <https://doi.org/10.1029/2020JB021627>, 2021.



- Xu, Z., Sun, L., Rahman, M. N. A., Liang, S., Shi, J., and Li, H.: Insights on the small tsunami from January 28, 2020, Caribbean Sea MW7.7 earthquake by numerical simulation and spectral analysis, *Natural Hazards*, <https://doi.org/10.1007/s11069-021-05154-1>, 2022.
- 610 Yamazaki, D., Ikeshima, D., Tawatari, R., Yamaguchi, T., O'Loughlin, F., Neal, J. C., Sampson, C. C., Kanae, S., and Bates, P. D.: A high-accuracy map of global terrain elevations, *Geophysical Research Letters*, 44, 5844–5853, <https://doi.org/10.1002/2017GL072874>, 2017.
- Yamazaki, Y., Lay, T., Cheung, K. F., Yue, H., and Kanamori, H.: Modeling near-field tsunami observations to improve finite-fault slip models for the 11 March 2011 Tohoku earthquake, *Geophysical Research Letters*, 38, <https://doi.org/10.1029/2011GL049130>, 2011.